Available online at www.sciencedirect.com
SCIENCE DIRECT®
ELSEVIER
International Journal of Solids and Structures 43 (2006) 3292–3305
INTERNATIONAL JOURNAL OF SOLIDS and STRUCTURES
www.elsevier.com/locate/ijsolstr

An analysis of the membrane deflection experiment used in the investigation of mechanical properties of freestanding submicron thin films

B. Peng, N. Pugno [1], H.D. Espinosa *

Department of Mechanical Engineering, Northwestern University, Evanston, IL 60208-3111, USA

Received 16 February 2005
Available online 22 September 2005

Abstract

In this paper we investigate, both experimentally and theoretically, the competition between different failure mechanisms (stretching, bending and curvature localization) in freestanding submicron thin films commonly used in micro-electromechanical systems. Microstructures made of elastic-brittle materials such as ultrananocrystalline diamond, diamond like carbon and silicon nitride, as well as elastic–plastic materials such as gold, aluminum, and copper, are tested by means of the membrane deflection experiment developed at Northwestern University. Evidence of competition between different failure modes has been found for the investigated elastic-brittle materials. The phenomenon is dependent on specimen size and shape. By contrast, in the case of elastic–plastic materials, failure due to stretching was found to be the dominant mechanism. An analytical model is proposed to rationalize the experimental data and to provide dimensionless parameters able to describe the competition between different failure mechanisms. These dimensionless parameters are particularly useful in the design of specimens employed in the MDE technique.

Keywords: Thin films; MEMS materials; Fracture; Plasticity; Nanoscale testing

1. Introduction

Thin films are customarily employed in micro-electronic components and micro-electromechanical systems (MEMS). Their properties frequently enable essential device functions. Therefore, accurate

* Corresponding author. Tel.: +1 847 467 5989; fax: +1 847 491 3915.
E-mail address: espinosa@northwestern.edu (H.D. Espinosa).
[1] On leave from Department of Structural Engineering, Politecnico di Torino, Italy.

0020-7683/$ - see front matter © 2005 Elsevier Ltd. All rights reserved.
doi:10.1016/j.ijsolstr.2005.07.052

identification of these mechanical properties is instrumental to the development of innovative technologies. To this effect, several testing techniques have been developed to study thin films and MEMS materials (e.g., Tsuchiya et al., 1996; Sharpe et al., 1997, 2003; Chasiotis and Knauss, 2002, 2000; Cho et al., 2005; LaVan et al., 2001; Espinosa et al., 2003a,b).

Tensile testing techniques were pioneered by Tsuchiya et al. (1996) and Sharpe et al. (1997, 2003). The test consists of stretching a freestanding thin film specimen fixed to the substrate at one end and connected to a large freestanding pad area at the other end. A probe is attached to the pad area for the purpose of applying load. The gripping techniques employed by the various groups were different and evolved over time. Tsuchiya et al. employed an electrostatic probe. This technique works well when the samples are thin and narrow in the gauge section because the electrostatic grip does not generate enough force to break relatively wide specimens. Sharpe et al. (1997, 2003) overcome this limitation by gluing the freestanding pad area of the specimen to a fiber (probe) using an ultraviolet curing adhesive. This procedure was first introduced by Chasiotis and Knauss (2000). The gluing method enables the application of large forces leading to specimen failure. However, alignment problems may adversely impact the testing results. Strains in the gauge region were measured by an interferometric technique. Chasiotis and Knauss (2002, 2000), Cho et al. (2005) used a similar specimen but with a slightly modified gripping method. In their investigation, tensile specimens were loaded by means of an inchworm actuator until failure. Digital image correlation (DIC), based on atomic force microscope (AFM) images, was employed to determine local strain fields. LaVan et al. (2001) used specimens fixed to the substrate at one end and possessing a ring with freely rotating pivot at the other end. The specimens were loaded with a micro-manipulator having a tungsten probe tip.

The variety of techniques used in the tensile testing of thin films clearly illustrates its complexity. Recently, a different test, known as membrane deflection experiment (MDE) was developed by Espinosa and coworkers. The technique involves the stretching of a free-standing thin film membrane in a fixed–fixed configuration with a double ''dog bone-like'' specimen shape. The geometry of the specimen is such that it contains tapered regions to eliminate boundary failure effects (Fig. 1). Several sizes of membrane specimens were designed on a single wafer (Table 1) to investigate size scale effects on film properties. The membrane is attached at both ends and spans a micro-machined window beneath. A nanoindenter is employed to apply a line-load, at the center of the span, to achieve specimen stretching. Simultaneously, an interferometer focused on the bottom side of the membrane records its deflection (Fig. 2). The result is direct tension of the gauge region. Further details of the experimental technique are given in Espinosa et al. (2003b). The main advantage of the MDE test is its simplicity, the independent measurement of stress and deflection, and its accuracy and repeatability. The technique was employed to investigate the mechanical properties of

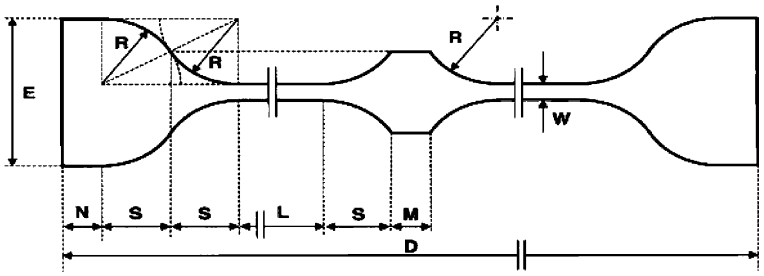

Fig. 1. Specimen with ''dog bone-like'' shape. The specimen thickness is h. For geometrical details and dimensions see (Espinosa et al., 2003b) and Table 1.

Table 1
Membrane dimensions for different sized specimens

Dimensions (μm)	Sample type						
	A	B	C	D	E	F	G
L	50	100	100	100	200	400	400
W	3	5	10	20	20	20	40
R	10	10	20	40	40	40	80
S	8.66	8.66	17.32	34.64	34.64	34.64	69.28
M	10	10	10	10	10	10	10
N	10	20	20	20	20	40	40
E	23	25	50	100	100	100	200

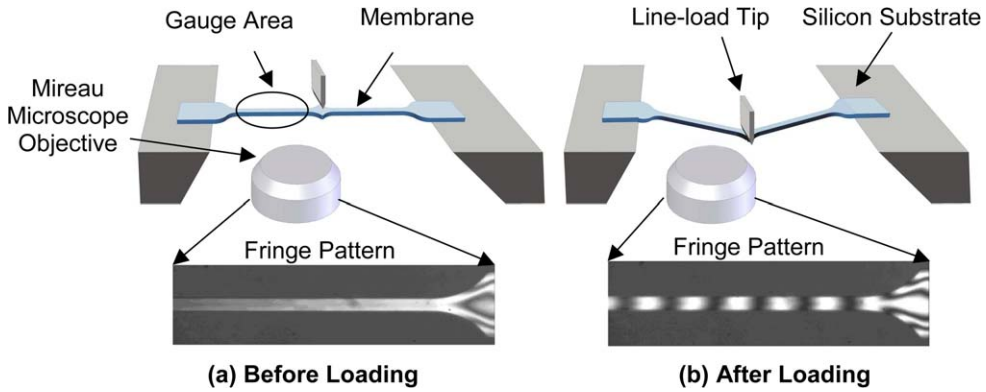

Fig. 2. Schematic drawing of the MDE setup and monochromatic images of the bottom side of a membrane in the unloaded state (a), and under load (b).

brittle and ductile materials in the form of submicron free-standing thin films (Espinosa et al., 2003a,b). Likewise, an extension of the MDE was employed to investigate fracture of MEMS materials (Espinosa and Peng, 2005) by introducing a sharp crack in the gauge region of the specimen, prior to its release, by means of micro-indentation.

A concern of the MDE test is the local bending of the specimen and its effect on material failure. Because of the specimen geometry, during the data reduction it is assumed that bending effects are localized and small, and that consequently they can be neglected. However, we have found that this assumption is not always valid. If the bending effect becomes important, as it may be the case for very stiff materials and certain specimen geometries (specimens with geometries C–E), a competition between bending and stretching is ensued. When the deflection is dominated by bending, the specimens fail in the middle of the span region where the load is applied. On the contrary, when the deformation is dominated by pure tension, the specimens fail in the gauge region, as intended. In this work, we discuss the competition of bending and stretching in MDE specimens of various materials and geometries. An analysis is presented to elucidate the experimental measurements and observations. The analysis confirms the existence of these competing failure mechanisms and provides dimensionless parameters that can be employed in the specimen design to avoid premature failure due to local or global bending.

2. Experimental observations

2.1. Elastic-brittle materials

Ultrananocrystalline diamond (UNCD), diamond like carbon (DLC), and silicon nitride (Si_3N_4) were tested as examples of elastic-brittle materials. The failure mechanism of these three materials was found to be very similar. As an example we discuss in detail the case of UNCD. The material displays a linear stress–strain response up to fracture. A similar stress–strain behavior was observed for DLC and Si_3N_4. The experimental results show that different failure modes occurred in different specimen geometries: *stretching mode* when failure occurred in the gauge region and *bending mode* when failure occurred in the middle of the span.

Fig. 3 shows the load–displacement and strain–stress curves, recorded optical fringes, and the specimen failure mode. The figure also shows fractographic details obtained by means of scanning electron microscopy (SEM) of the fracture surfaces. Fig. 3a–e correspond to specimen type G, while Fig. 3f–j correspond to specimen type E. The load–displacement curves (Fig. 3a and f) are of a cubic form, as a consequence of the large displacements imposed to the thin film (see Section 3). The strain–stress curves (Fig. 3b,g) are linear up to failure (note that the stresses and strains are calculated—see Section 3—in the gauge region, so their maximum values are not necessarily indicative of the strength of the material if failure occurs in bending mode). A Young's modulus of 0.96 TPa and a fracture strength of 4.23 GPa (Fig. 3b) were observed for UNCD. The interferometric images reported in Fig. 3c and h show that the strain is uniform in the gauge region. The SEM images (Fig. 3d and i) show the existence of two failure modes. High magnification SEM imaging of the UNCD fracture surfaces reveals similarities with those observed in ceramic materials (Fig. 3e and j); namely, they exhibit a roughness comparable to the size of the grain clusters formed in the growth process (Espinosa et al., submitted for publication). Failure initiates from defects in the film and propagates between clusters.

From the stress–strain curve corresponding to the specimen exhibiting bending failure mode (Fig. 3f), the elastic modulus is again 0.95 TPa. The maximum load was measured to be 5.07 mN and the *apparent* strength 2.58 GPa. The interferometric optical fringes (Fig. 3h) show that the local strain in the middle of the span, region where the line load is applied, appears not uniform. Fracture occurs in this region and the fracture surface exhibits a kink. Similar features were observed in DLC and Si_3N_4 for the same type of specimen.

Fracture properties and strength stochasticity of UNCD thin films, without (Espinosa et al., 2003a) and with sharp or blunt cracks and re-entrant corners (Espinosa and Peng, 2005; Pugno et al., 2005) have been investigated using the MDE technique. In these investigations, sample dimensions leading to stretching failure mode were exclusively employed.

2.2. Elastic–plastic materials

The failure features observed in ductile materials are different from those previously discussed (Espinosa et al., 2004). Gold, aluminum and copper thin films with various geometries were tested under the same conditions. All films were deposited by e-beam evaporation. No specimen was found to fail in bending mode. In this case, compatible film deflection is accomplished by development of plastic hinges at the fixed ends and in the middle of the span. Hence, the risk of failure due to bending is reduced. In Fig. 4, the same experimental results, previously discussed for the case of brittle materials are reported for the case of elastic–plastic materials (in particular for copper). The load–diplacement and strain–stress curves of a 1 μm thick copper membrane with dimension E are given in Fig. 4a and b. A typical elastic–plastic behavior is observed. The Young's modulus was measured to be 121 GPa; the yielding stress was about 250 MPa, whereas the failure stress is close to 465 MPa. The material exhibits a very high hardening rate and fails

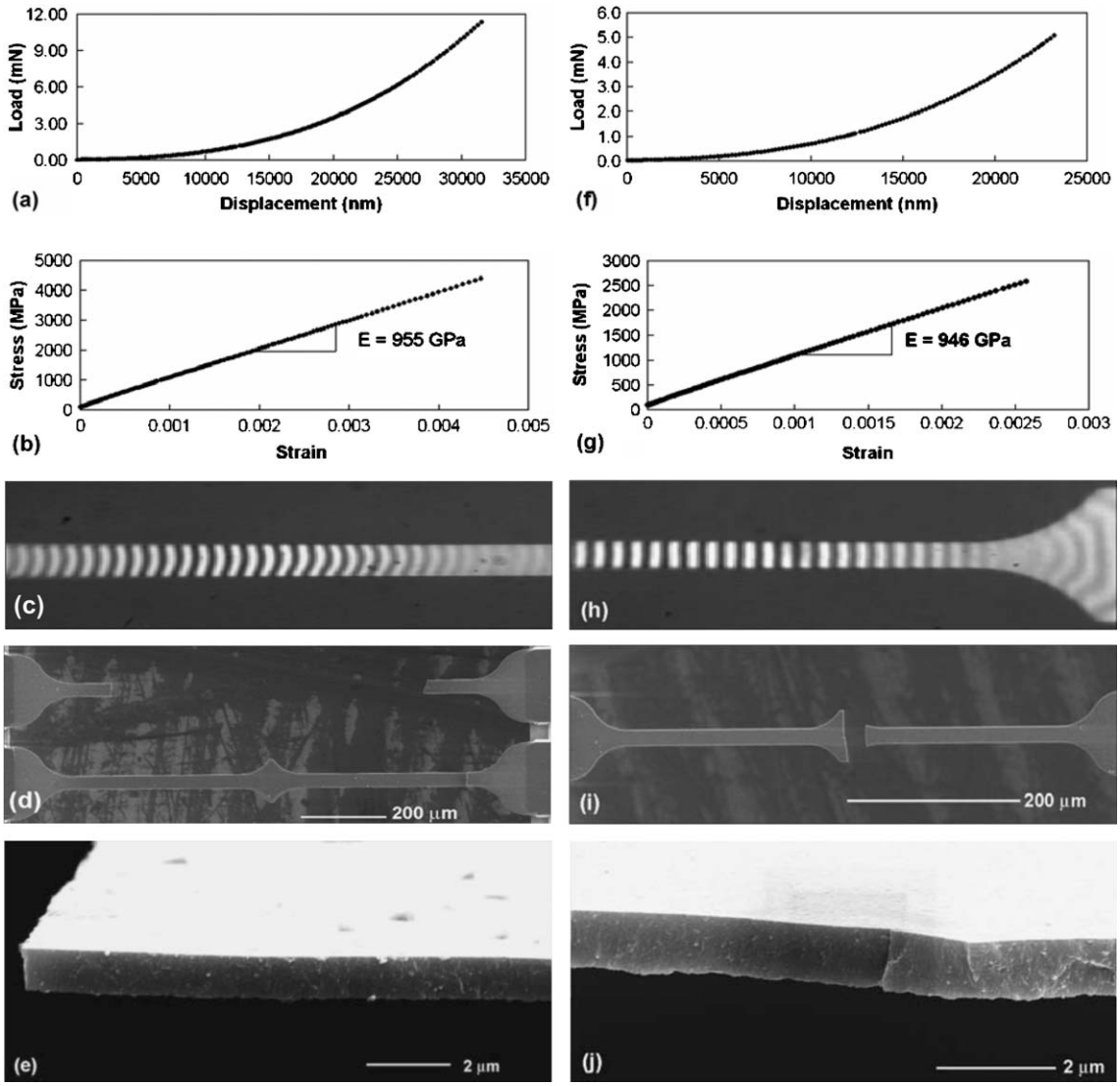

Fig. 3. Example of experimental results of elastic-brittle materials (UNCD) exhibiting stretching (left) and bending (right) failure modes: load–displacement (a) and (f), and stress–strain curves (b) and (g); optical fringes before failure (c) and (h) (note equal fringe spacing, i.e., uniform deformation of the specimen); broken specimen (d) and (i) and crack surface (e) and (j).

at relatively small strains. By examining the value of the stress at zero strain, the residual stress resulting from the micro-fabrication process is estimated to be around 50 MPa. The interferometric optical fringes clearly show failure in the gauge region (Fig. 4c). Fracture occurs in this region (Fig. 4d) indicating that tension dominates the failure competition. Fig. 4e is a high magnification SEM image of the failure region. Several features are apparent: the fracture exhibits a complex path with some clear changes in direction and the surface near the fracture is very smooth. The failure of the membrane can consequently be described as quasi-brittle in nature. Similar observations were made in Au specimens for thicknesses of 0.3 and 0.5 μm.

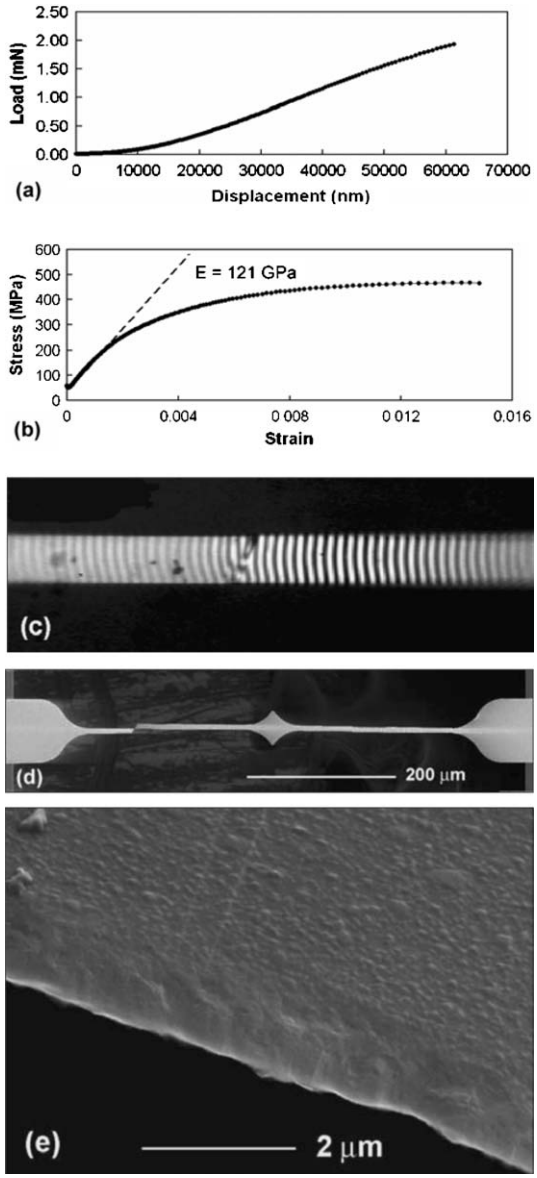

Fig. 4. Example of experimental results for elastic–plastic materials (copper) exhibiting stretching failure mode: load–displacement (a); stress–strain curve (b); optical fringes before failure (c) (discontinuities consistent with shear localization in the specimen); broken specimen (d) and failure zone (e).

3. Analytical analysis

3.1. Stretching under large displacements

Membrane deflection experiments are usually described by a three hinge model (Espinosa et al., 2003a,b) (Fig. 5). In this model, a specimen of length l in the undeformed configuration is mapped to a new

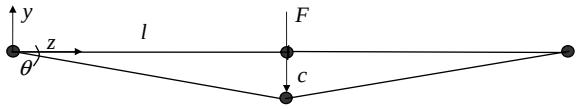

Fig. 5. Three hinges model for MDE data reduction.

configuration. If we use the rotation ϑ to describe this configuration, the stretching, ε_s, under large displacements (see Fig. 5) is simply given by

$$\varepsilon_s = \frac{l/\cos\vartheta - l}{l} = \frac{1-\cos\vartheta}{\cos\vartheta}. \tag{1}$$

This equation represents a compatibility condition. In the linear elastic regime, the corresponding stress σ_s is

$$\sigma_s = E\varepsilon_s = E\left(\frac{1-\cos\vartheta}{\cos\vartheta}\right), \tag{2}$$

where E is the Young's modulus. On the other hand, the central (vertical) displacement under the applied load F is

$$c = l\tan\vartheta, \tag{3}$$

and the corresponding tension T in the specimen is

$$T = \frac{F}{2\sin\vartheta}. \tag{4}$$

This equation represents the equilibrium condition. The corresponding stress is

$$\sigma_s = \frac{T}{A} = \frac{F}{2A\sin\vartheta}, \tag{5}$$

where $A = Wh$ is the film cross sectional areas, W its width, and h its height.

The stress–strain curve, according to Eq. (2), is expected to be linear only in the linear elastic regime. On the other hand, the force versus displacement can be obtained by equating Eqs. (2) and (5) and by employing Eqs. (3) and (4), namely,

$$F = 2EA\left(\frac{1-\cos\left(\tan^{-1}\frac{c}{l}\right)}{\cos\left(\tan^{-1}\frac{c}{l}\right)}\right)\sin\left(\tan^{-1}\frac{c}{l}\right). \tag{6}$$

For moderately large displacements ($\sin\vartheta \approx \tan\vartheta \approx \vartheta, \cos\vartheta \approx 1-\vartheta^2/2$), Eq. (6) becomes:

$$F = \frac{EA}{l^3}c^3. \tag{7}$$

As a consequence, the force–displacement curve is expected to be of a cubic form in the linear elastic regime. The experimental results clearly show this cubic form (Fig. 3a).

3.2. Curvature localization

The previously discussed mode of deformation implies curvature localization rather than a bending deformation distributed along the length of the specimen. In this section we investigate the possibility of failure in such region rather than in the homogeneously stretched regions.

Localization of curvature in the central zone clearly occurs as imposed by deformation compatibility. The problem is of an imposed large rotation ϑ in a localized zone of length, l_c, Fig. 6. The corresponding (mean) curvature is

$$\chi = \frac{\vartheta}{l_c}. \tag{8}$$

This equation is a compatibility condition.

The curvature is estimated through its mean value. In addition, it is interesting to note that the real curvature is close to a constant as a consequence of the tapering in the central region of the specimen. For a triangular tapering it is theoretically a constant.

Accordingly, we can estimate the maximum strain at the external fibers, $y = \mp h/2$, as:

$$\varepsilon_c = \frac{h}{2l_c}\vartheta. \tag{9}$$

In the linear elastic regime, the corresponding stress is

$$\sigma_c = E\varepsilon_c = E\frac{h}{2l_c}\vartheta. \tag{10}$$

On the other hand, the moment in the central cross-section, Fig. 6, due to the tension T in the film is given by,

$$M_c = \frac{F}{2}l_c\frac{\sin\vartheta}{\cos\vartheta} - \frac{F}{2\tan\vartheta}\frac{1}{\chi}(1-\cos\vartheta) \cong \frac{F}{2}l_c - \frac{F}{2\vartheta}\frac{l_c}{\vartheta}\frac{\vartheta^2}{2} = \frac{F}{4}l_c. \tag{11}$$

The second term in the above equation is a consequence of the large displacements and rotations. Eq. (11) represents an equilibrium condition. The corresponding maximum stress is

$$\sigma_c = \frac{6M_c}{bh^2} = \frac{3Fl_c}{2bh^2}, \tag{12}$$

where b is the specimen width in the central cross-section of the specimen, which is micro-fabricated larger than W for a better distribution of the applied load.

By equating Eqs. (10) and (12) we obtain the length in which the localization in curvature occurs, i.e.,

$$l_c^2 = \frac{Ebh^3\vartheta}{3F}. \tag{13}$$

We can estimate the length l_c starting from the experimental values of F and ϑ (from which also E can be deduced). This analysis provides values of few microns for the curvature localization zone.

Finally, substituting Eq. (13) into Eq. (10) or Eq. (12) provides the stress due to curvature localization, viz.,

$$\sigma_c = \sqrt{\frac{3EF\vartheta}{4bh}}. \tag{14}$$

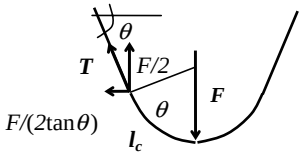

Fig. 6. Curvature localization in the applied load region.

3.3. Competition between stretching and curvature localization

The axial stresses given by Eqs. (2) and (5) and that of curvature localization given by Eq. (14), under the assumption of moderately large displacements, are

$$\sigma_s^2 \approx \frac{E}{2}\vartheta^2\frac{F}{2\vartheta Wh} = \frac{EF\vartheta}{4Wh}, \quad \sigma_c^2 = \frac{3EF\vartheta}{4bh}. \tag{15}$$

Accordingly, we can define a dimensionless parameter describing the competition between stretching and curvature localization as:

$$\lambda_{sc} = \frac{\sigma_s}{\sigma_c} \approx k_1\sqrt{\frac{b}{W}}, \tag{16}$$

where k_1 is an experimental constant (under our simplified hypothesis, e.g., constant concentrated curvature, $k_1 \approx 1/\sqrt{3}$). For $\lambda_{sc} \gg 1$ the prevalent failure mechanism is stretching, vice versa for $\lambda_{sc} \ll 1$ curvature localization would prevail. The experimentally investigated specimen geometries exhibited $b \approx 3W$; thus, this competition does not appear to be the reason for the observed failure mode transition between stretching and bending.

3.4. Competition between stretching and bending

In Section 3.1 we have assumed a mode shape corresponding to pure stretching. The complementary assumption corresponds to a mode shape of pure bending, i.e.,

$$w = \left[-2\left(\frac{z}{l}\right)^3 + 3\left(\frac{z}{l}\right)^2\right]c, \tag{17}$$

where $0 \leqslant z \leqslant l$ is the axial co-ordinate starting from one fixed end and c is the central deflection. However, associated to this mode shape, stretching stresses and strains under large displacement arise. We study only half of the structure as a consequence of the symmetry.

To take into account the nonlinear effect of large displacements, we evaluate the energy stored in the beam not only due to bending but also due to stretching.

The strain due to bending is Carpinteri et al. (1997):

$$\varepsilon_b = -y\frac{d^2w}{dz^2}, \tag{18}$$

where y is a *central* co-ordinate (along a *principal direction* of the inertia tensor and with origin in the centroid of the cross-section), parallel to the direction of the applied force. Substituting Eq. (17) into Eq. (18) gives:

$$\varepsilon_b = 6\left(2\frac{z}{l} - 1\right)\frac{cy}{l^2}. \tag{19}$$

The maximum value is reached at the external fibers where $y = \mp h/2$. The absolute maximum is

$$\varepsilon_{b\,max} = 3\frac{ch}{l^2}, \tag{20}$$

and occurs at the coordinates $z = 0, l$ (i.e., at the fix ends and in the middle of the span).

In addition, the strain due to stretching is (a more significant estimation would be given by the mean value of Eq. (21), but this is irrelevant for our purpose):

$$\varepsilon_s \approx \frac{1}{2}\left(\frac{dw}{dz}\right)^2. \tag{21}$$

Substituting Eq. (17) into Eq. (12) yields:

$$\varepsilon_s = 18\left[\left(\frac{z}{l}\right)^4 - 2\left(\frac{z}{l}\right)^3 + \left(\frac{z}{l}\right)^2\right]\frac{c^2}{l^2}. \tag{22}$$

Its maximum value will be reached at the point $z = l/2$ (i.e., in the gauge region):

$$\varepsilon_{s\max} = \frac{9}{8}\frac{c^2}{l^2}. \tag{23}$$

Note that the result of $\varepsilon_s \propto c^2/l^2$ is consistent with that of Eq. (1), under the assumption of moderate displacements.

The ratio between the stresses due to stretching and bending defines a second dimensionless parameter describing the competition between stretching and bending:

$$\lambda_{sb} = \frac{\sigma_s}{\sigma_b} = \frac{\varepsilon_{s\max}}{\varepsilon_{b\max}} = \frac{3}{8}\frac{c}{h}. \tag{24}$$

From Eq. (23), $c_u \approx l\sqrt{8\varepsilon_u/9}$, so that:

$$\lambda_{sb} = k_2\frac{l}{h}\sqrt{\varepsilon_u}, \tag{25}$$

where k_2 is a constant that can be deduced from one experiment. From the UNCD data, we identify $k_2 \approx 1/26$. Note that k_2 cannot be determined theoretically (at least by this analysis), since it would depend on the assumed mode shape for w. However, the validity of the result of Eq. (25) is general, since different mode shapes would result only in different value of k_2. We close this subsection by noting that for $\lambda_{sb} \gg 1$, the predominant failure mechanism is stretching, and vice versa, for $\lambda_{sb} \ll 1$, bending prevails. The analysis rationalizes the reason for the observed differences in failure mode (stretching vs. bending) as a function of specimen dimensions.

3.5. Alternative analytical approach: the elastic line equation

Another approach is used to confirm the analyses previously reported for the two predominant mechanisms of stretching and bending (Sections 3.1 and 3.4). Since the problem cannot be solved in closed form, we make reasonable assumptions. Instead of assuming a mode-shape and deriving the tension, as previously done (Sections 3.1 and 3.4), in this section we assume a constant tension T, deriving the corresponding correct mode shape by solving the elastic line equation of a beam (Carpinteri et al., 1997). This procedure was proposed in (Sapmaz et al., 2003).

The elastic line equation is

$$EIw'''' - Tw'' = F\delta(z - l), \tag{26}$$

where $I = Wh^3/12$ is the moment of inertia and the symbol "′" corresponds to the derivate with respect to z. Assuming $T =$ const. and applying the boundary conditions ($w(z = 0, 2l) = w'(z = 0, 2l) = 0$), the symmetric solution of Eq. (26) is

$$w(z) = \frac{F\sqrt{EI}}{2T^{3/2}}\left(\tanh\left(\sqrt{\frac{T}{EI}}l\right)\left(\cosh\sqrt{\frac{T}{EI}}z - 1\right) - \sinh\sqrt{\frac{T}{EI}}z + \sqrt{\frac{T}{EI}}z\right) \quad 0 \leqslant z \leqslant l. \tag{27}$$

The tension, assumed as a constant, can be obtained self-consistently by the mean value of Eq. (21) as

$$T = \frac{EA}{2}\int_0^l w'^2\,\mathrm{d}z. \tag{28}$$

The results are

$$T = \frac{F^2 l^4 A}{1920 EI^2}; \quad T \ll \frac{EI}{4l^2}, \tag{29a}$$

$$T = \frac{1}{2}\left(EAF^2\right)^{\frac{1}{3}}; \quad T \gg \frac{EI}{4l^2}. \tag{29b}$$

We note that these results are consistent with the previous analysis. Indeed:

(1) for large stretching ($T \gg \frac{EI}{4l^2}$) the solution of the tension is exactly the same as the one derived in Section 3.1, assuming the simple three hinge model (as it is simple to verify rearranging the formulas and assuming moderate displacements). Hence, the classical approach applied in the study of MDE is confirmed. Note in addition that, this analysis shows that the tension in the bending regime (small load) should be estimated with the expression reported in Eq. (29a), rather than with Eq. (29b).
(2) the crossover between bending regime ($T \ll \frac{EI}{4l^2}$) and stretching regime ($T \gg \frac{EI}{4l^2}$) arises for $\lambda \approx \sqrt{\frac{Tl^2}{EI}}$ equal to a constant. At the competition, $T \approx \sigma_u A$, so that $\lambda \propto \frac{l}{h}\sqrt{\varepsilon_u}$, which represents the same form deduced for λ_{sb} in Eq. (25). Note that also from this approximated analysis (e.g., as a consequence of the hypothesis $T = \text{const.}$) the value of k_2 cannot be deduced, and must be considered an experimental value.

4. Experimental and analytical comparison

In the membrane deflection experiment, the central vertical displacement c and the applied force F by the nanoindenter are measured. Some examples of force vs. displacement are reported in Figs. 3 and 4a, as previously discussed. According to our analytical analysis, the angle ϑ is evaluated from Eq. (3), the stress from Eq. (5) and the strain from Eq. (1). Note that this procedure does not assume a priori a particular constitutive law (e.g., linear elastic), so that experimentally stress–strain curves without material restriction (e.g., for linear elastic–plastic materials) can be obtained. As previously discussed, examples of computed stress–strain curves for brittle and plastic materials are reported in Fig. 3b and Fig. 4b, respectively. The optical fringes (recorded by the Interferometer Microscope) are used to define when the test begins, i.e., when the contact between nanoindenter and specimen is reached, to have an independent measurement of the displacements and to visualize the occurrence of strain localizations and/or fracture. The interference fringes for brittle materials exhibiting bending failure mode (Fig. 3h) do not show any unusual pattern until abrupt failure occurs (Fig. 3i). On the other hand, for elastic–plastic materials, a strain localization in the middle of the gauge region (Fig. 4c), is manifested by a discontinuity in the fringes. Failure then occurs in this region (Fig. 4d). The failure localization is not observed in elastic-brittle materials even for stretching failure mode (Fig. 3d). Failure occurs catastrophically as expected.

Relevant experimental results are reported in Table 2, where the mean values of the ultimate stresses and strains, yield stress, and Young's modulus are reported for the different investigated elastic-brittle and elastic–plastic materials. The ultimate strain is used as a dimensionless parameter to describe the material according to the dimensionless parameter of Eq. (25).

Table 2
Mean values for the ultimate (u) and yield (y) stress and strain and Young's modulus for the investigated elastic-brittle and elastic–plastic materials

	σ_u [MPa]	ε_u	σ_y [MPa]	ε_y	E [GPa]
UNCD	4280	0.0040	–	–	955
DLC	5372	0.0066	–	–	820
Si_3N_4	1510	0.0040	–	–	305
Gold	305	0.080	251	0.038	54
Aluminum	244	0.030	204	0.006	65
Copper	799	0.014	390	0.003	121

Table 3
Competition between stretching and bending failure modes for the investigated elastic-brittle and elastic–plastic materials: in all cases ($b/W \approx 3$) and dimensionless competing parameter ($k_2 \approx 1/26$)

Material	L [μm]	l [μm]	W [μm]	h [μm]	Stretching	Bending	λ_{sb}
UNCD	100	224	20	0.8	No	Yes	0.45
	200	324	20	1.2	Yes	Yes	0.98
	400	628	20	1.0	Yes	No	1.53
DLC	100	224	20	1.2	No	Yes	0.42
	200	324	20	1.2	Yes	Yes	0.92
	400	628	20	1.2	Yes	No	1.40
Si_3N_4	100	224	20	0.5	Yes	Yes	1.09
	200	324	20	0.5	Yes	No	2.37
	400	628	20	0.5	Yes	No	3.61
Gold	50	96	3	0.3	Yes	No	3.48
	100	146	5	0.3	Yes	No	5.29
	200	272	10	0.3	Yes	No	9.86
Aluminum	100	172	10	0.3	Yes	No	1.14
	100	172	10	1.0	Yes	No	1.30
	200	324	20	1.0	Yes	No	2.15
Copper	100	146	5	0.2	Yes	No	3.32
	100	172	10	0.2	Yes	No	7.37
	200	324	20	0.2	Yes	No	14.74

L is the length of the gauge region (Fig. 1) different from the total half-length l of the specimen (Figs. 1 and 5).

Three different geometries for each of the three different investigated elastic-brittle (UNCD, DLC, Si_3N_4) and elastic–plastic materials (gold, aluminum and copper) are reported in Table 3. In this table each material and specimen geometry are specified and the corresponding dimensionless parameter is evaluated. The experimental observations for the two different failure modes are also emphasized (in the table "yes" means that we have observed the corresponding failure mode and "no" that we did not observe it). In agreement with our analysis the stretching was observed when $\lambda_{sb} \gg 1$, whereas for $\lambda_{sb} \ll 1$ bending prevailed. In some cases, for the same geometry and material, both stretching and bending failure modes were observed (in correspondence of $\lambda_{sb} \approx 1$), resulting in completely different force vs. displacement and stress–strain curves, as shown in Fig. 7. In this case, one specimen failed simultaneously at the two gauge regions (failure stress = 4.67 GPa) while another one failed at the center of the span (failure stress = 2.58 GPa). One of the tested Aluminum specimens is found to be close to a bending failure mode. Indeed the specimen exhibit a brittle failure (Espinosa et al., 2004). The larger values of this parameter for the majority of the elastic–plastic specimens represent the reason for which the bending failure mode was not observed.

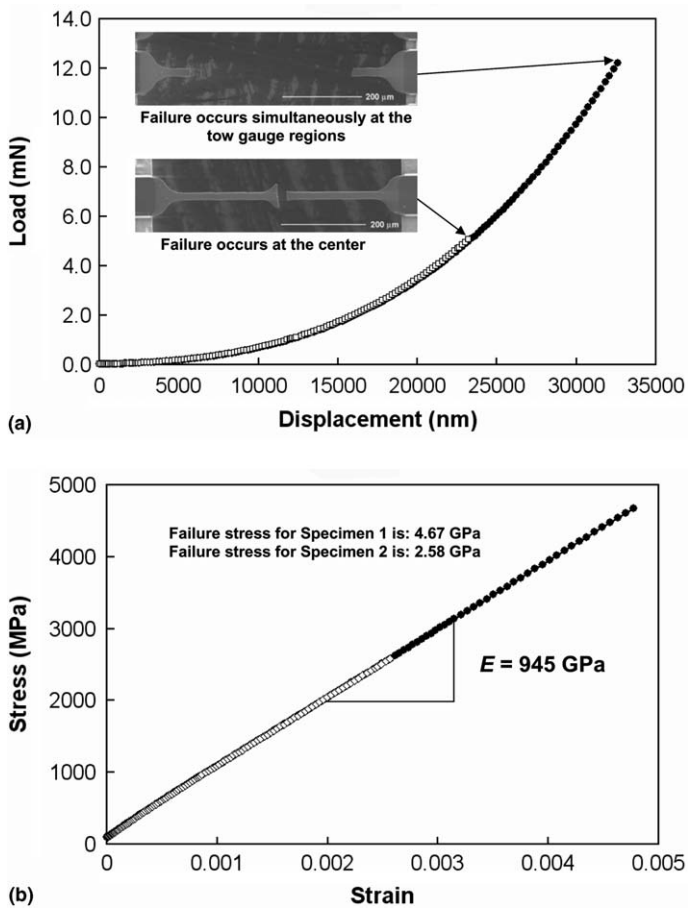

Fig. 7. Comparison between force–displacement (a) and stress–strain curves (b) for specimens exhibiting different failure modes even when geometry and material are identical (UNCD, sample type E, $l = 324$ μm).

5. Conclusions

In this paper we report experimental evidence of the competition between different failures mechanisms observed in freestanding submicron thin films tested by means of the membrane deflection experiment. The dominant failure mode was found to be stretching—for each investigated size and shape—only for elastic–plastic materials. By contrast, for elastic-brittle materials both failure modes were observed, as a function of the size and shape of the specimen. An analytical model is discussed to rationalize these observations in terms of dimensionless parameters, which accurately characterizes the physics of the problem. Even when the curvature localization was not identified as the reason for observed failure mode transition ($b/W \approx$ const.), the derived dimensionless parameter of Eq. (16) suggests that the ratio b/W should be large enough to avoid failure due to a localization of curvature, at least for brittle materials, for which the development of plastic hinges cannot take place.

In summary, the derived parameters should be used as a guide in the design of MDE specimens to achieve failure in pure tension. This optimized specimen design simplifies the experimental investigation by the MDE technique when brittle materials or ductile materials that may exhibit high yield stresses

due to size scale effects are studied. These materials, e.g., diamond, silicon carbide, metal alloys, shape memory alloys and nano composites, are increasingly being employed in MEMS/NEMS applications.

Acknowledgements

This work was sponsored by the National Science Foundation under NIRT award no. CMS-9624364 and under GOALI award no. CMS-0120866. Work was also supported in part by the Nanoscale Science and Engineering Initiative of the National Science Foundation under NSF award no. EEC-0118025 and by DOE Office of Science under contract no. N00014-97-1-0550. We thank O. Auciello, J. Carlisle and D. Gruen for providing the UNCD films, and Sandia National Laboratory for providing the amorphous diamond films. The authors would like to acknowledge R.S. Divan and N. Moldovan for assistance in the micro-fabrication of the specimens.

References

Bagdahn, J., Sharpe, W.N., 2003. Fracture strength of polysilicon at stress concentrations. Journal of Electromechanical Systems 12, 302–312.

Carpinteri, A., 1997. Structural Mechanics: A Unified Approach. E&FN Spon, 1997.

Chasiotis, I., Knauss, W.G., 2002. A new microtensile tester for the study of MEMS materials with the aid of atomic force microscopy. Experimental Mechanics 42 (1), 51–57.

Chasiotis, I., Knauss, W.G., 2000. Microtensile Tests with the aid of Probe Microscopy for the study of MEMS materials. SPIE Proceedings 4175, 96–103.

Cho, S.W., Chasiotis, I., Friedman, T.A., Sullivan, J., 2005. Direct measurements of Young's modulus, Poisson's ratio and failure properties of ta-C MEMS. Journal of Micromechanics and Microengineering 25 (4), 728–735.

Espinosa, H.D., Peng, B., 2005. A new methodology to investigate fracture toughness of freestanding MEMS and advanced materials in thin film form. Journal of Microelectromechanical Systems 14, 153–159.

Espinosa, H.D., Peng, B., Prorok, B.C., Moldovan, N., Auciello, O., Carlisle, J.A., Gruen, D.M., Mancini, D.C., 2003a. Fracture strength of ultrananocrystalline diamond thin films-identification of Weibull parameters. Journal of Applied Physics 94, 6076–6084.

Espinosa, H.D., Prorok, B.C., Fischer, M., 2003b. A methodology for determining mechanical properties of freestanding thin films and MEMS materials. Journal of the Mechanics and Physics of Solids 51, 47–67.

Espinosa, H.D., Prorok, B.C., Peng, B., 2004. Plasticity size effects in free-standing submicron polycrystalline FCC films subjected to pure tension. Journal of the Mechanical Physics of Solids 52, 667–689.

Espinosa, H.D., Peng, B., Moldovan, N., Friedmann, T.A., Xiao, X., Mancini, D.C., Auciello, O., Carlisle, J., Zorman, C.A., Merhegany, M., submitted for publication. Elasticity, strength and toughness of three novel MEMS/NEMS materials – 3C-SiC, UNCD, ta-C. Small.

LaVan, D.A., Jackson, K., Glass, S.J., Friedmann, T.A., Sullivan, J.P., Buchheit, T., 2001. Direct Tension and Fracture Toughness Testing Using the Lateral Force Capabilities of a Nanomechanical Test System. In: Muhlstein, C., Brown, S.B. (Eds.), Mechanical Properties of Structural Films, ASTM STP 1413. American Society for Testing and Materials, West Conshohocken, PA.

Pugno, N., Peng, B., Espinosa, D., 2005. Predictions of strength in MEMS components with defects –a novel experimental–theoretical approach. Journal of Solids and Structures 42, 647–661.

Sapmaz, S., Blanter, Ya.M., Gurevich, L., van der Zant, H.S.J., 2003. Carbon nanotubes as nanoelectromechanical systems. Physical Review B 67, 1–235414-1/7.

Sharpe Jr., W.N., Yuan, B., Edwards, R.L., 1997. A new technique for measuring the mechanical properties of thin films. Journal of Microelectromechanical systems 6 (3), 193–199.

Tsuchiya, T., Tabata, O., Sakata, J., Taga, Y., 1996. Tensile testing of polycrystalline silicon thin films using electrostatic force grip. Transaction of the Institute of Electrical Engineers of Japan 116, 441–446.